A Comparison of Turbulence Ingestion of Axisymmetric and Non-Axisymmetric Wakes Into a Rotor

Conference Paper · January 2022

DOI: 10.2514/6.2022-2528

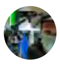

Jarrod Banks
Virginia Tech (Virginia Polytechnic Institute and State University)

Humza Butt
Virginia Tech (Virginia Polytechnic Institute and State University)

N. Agastya Balantrapu
University of Utah

Christopher Hickling
Virginia Tech (Virginia Polytechnic Institute and State University)

AIAA SciTech Forum
January 3-7, 2022, San Diego, CA & Virtual
AIAA SCITECH 2022 Forum
10.2514/6.2022-2528

Check for updates

A Comparison of Turbulence Ingestion of Axisymmetric and Non-Axisymmetric Wakes Into a Rotor

Jarrod T. Banks *, Humza Butt †, William J. Devenport ‡, and William N. Alexander §
Center for Research in Experimental Aero/Hydrodynamic Technology, Blacksburg, VA,24060

N. Agastya Balantrapu ¶
Princeton University, Princeton, NJ, 08544

Christopher J. Hickling ‖
Naval Surface Warfare Center, Carderock, MD, 20817

Stewart Glegg**
Florida Atlantic University, Boca Raton, FL, 33431

Measurements of a turbulent boundary layer ingested into a rotor at the aft of a body of revolution inclined at angle of attack were taken. Velocity fields and acoustic measurements were taken and the results compared to previous axisymmetric flow studies. Three dimensional effects from the non-axisymmetric nature of the flow were found to significantly influence the turbulence levels and thrusting profile of the rotor. Changes in rotor angle relative to the observer from the non-axisymmetry produced as much as a 5 dB increase in the sound produced, and haystacking at blade multiples was observed in the sound spectrum.

I. Nomenclature

α	=	angle of attack (degrees)
δ	=	boundary layer thickness (mm)
D	=	body of revolution diameter (mm)
dB	=	decibels relative to $20\mu Pa$
f	=	frequency (Hz)
G	=	autospectrum (dB/Hz)
J	=	advance ratio
RPM	=	revolutions per minute

*Graduate Research Associate, Center for Research in Experimental Aero/Hydrodynamic Technology, AIAA Student Member
†Graduate Research Associate, Center for Research in Experimental Aero/hydrodynamic technology, AIAA Student Member
‡Professor, Center for Research in Experimental Aero/Hydrodynamic Technology, Associate Fellow AIAA.
§Assistant Professor, Center for Research in Experimental Aero/Hydrodynamic Technology, Associate Fellow AIAA.
¶Assistant Professor, Princeton University, AIAA Member
‖Research Scientist, Naval Surface Warfare Center, AIAA Member.
**Professor, Department of Ocean and Mechanical Engineering, Associate Fellow AIAA.

X, Y, Z = test section fixed coordinate system

x, y, z = body fixed coordinate system

U = velocity (m/s)

u = fluctuating velocity (m/s)

Subscripts

e = edge

∞ = infinity

X, Y, Z = test section fixed coordinate system

x, y, z = body fixed coordinate system

II. Introduction

In many engineering applications, rotors are required to interact with turbulence. This turbulence excites unsteady loading on the rotor blades that can radiate as sound to the far field, resulting in unwanted community noise or vehicle detection. The impact of turbulence ingestion noise (TIN) is exacerbated if the turbulence is of sufficient scale to produce unsteady loads which are correlated from blade-to-blade (i.e. if the convecting turbulent structures are cut multiples times by the rotor blades as they pass through the rotor disc plane). In this case, broadband humps or haystacks appear in the loading and consequently noise spectra at the blade passage frequency and its harmonics. Sevik [1] was among the first to observe this phenomenon, and significant research over several decades resulted in successful modeling of the blade-to-blade correlation effects and prediction of the haystacking phenomenon for homogeneous, isotropic turbulence [2]. The work of Hanson [3], Majumdar and Peake [4], and Atassi and Logue [5] to name a few, has emphasized the importance of flow anisotropy on haystacking and shown that haystacking can be greatly enhanced when the turbulence is distorted as it is drawn into a thrusting rotor. Recently, the work of Catlett and Anderson [6], [7] shows the effects of inhomogeneity and non-stationarity on TIN predictions. In all flow cases, accurate prediction of TIN and the haystacking phenomenon requires detailed knowledge of the turbulent inflow seen by the rotor and the unsteady loading response of the blades to that inflow.

In particular, the first major step in analytic TIN predictions is to model the two-point space time correlation function of the rotor inflow as a function of rotor operating condition. Commonly this is achieved in two steps: First, a space-time correlation model, usually for homogeneous, isotropic turbulence, is modified to match the flow of interest, based on measurements of a subset of the two-point velocity correlation structure, made without the rotor. Second, given the mean flow field leading up to the rotor face, Rapid Distortion Theory (RDT) based modelling is used to distort the developed model correlation as a function of the rotor advance ratio, resulting in the two-point correlation function seen by the rotor blades. With this final rotor inflow model, the unsteady loading is predicted with an analytic blade response function, and the resulting sound propagated to the far field with an appropriately chosen Green's function. Validating the distortion modeling independently of the blade response and propagation modelling for complex rotor geometries is challenging as it requires detailed two-point velocity measurements in front of a spinning rotor. Such measurements have been occasionally accomplished, mostly with blade mounted hotwire probes and unsteady surface pressure sensors, but these discrete sensor based approaches suffer from limited spatial resolution due to space constraints within the rotor combined with the difficulty in routing sensor power and signal from the rotating instrumentation into a fixed frame.

In this paper, we will present the preliminary measurements of the space-time structure (3-component velocity, space and time) of the inflow to a rotor at the rear of an axisymmetric body of revolution (BOR) inclined at an angle to the flow, as a function of the rotor thrust. This was achieved with a 25 kHz time-resolved stereoscopic Particle Image Velocimetry system imaging the instantaneous structure of the inflow to the rotor disk. Extending the prior work on a five-bladed subsonic rotor ingesting an axisymmetric turbulent boundary layer (TBL) by Hickling et al. [8], and the space-time structure of the flow around an axisymmetric body of revolution by Balantrapu A. N. [9]. The measurements will be compared at various thrusting conditions. Furthermore, by synchronously measuring the far-field acoustics of the rotor with a 251 phased microphone-array, we are developing a direct insight into the physics of turbulence ingestion noise.

There are significant three dimensional effects that arise from inclining a body of revolution at an angle of attack. Kumar and Prasad [10], Tinling and Allen [11], and Rodgers [12] describe the presence of a pair of asymmetric, counter-rotating vortices that develop on the leeward side of a body of revolution when inclined at an angle of attack. These vortices are likely to have significant effects on the turbulence in the turbulent boundary layer as will be shown in Section IV.

This project is a part of a larger effort aimed at developing analytical Turbulence Ingestion Noise prediction tools. Additionally, we hope to obtain fundamental insight into the rotor noise mechanisms through simultaneous measurements of the ingested inflow and corresponding acoustic far-field.

III. Experimental Methods

A. Wind Tunnel

All measurements were carried out in the Virginia Tech Stability Wind Tunnel in its anechoic configuration. In this configuration, the side walls of the 1.85-m square by 7.32 m long test section (Fig 1) are formed by 4.2 m long Kevlar windows that both contain the flow and allow sound to radiate from the test section to 6 m by 2.8 m by 4.2 m anechoic chambers where microphone instrumentation is placed. The floor and ceiling of the test section are made up of Kevlar-covered perforated aluminum panels backed with acoustic absorbing foam wedges. The facility is anechoic down to 180 Hz and the free stream turbulence levels are very low: 0.021 % at 21 m/s where all measurements are being made. The facility is described in detail by Devenport et al. [13].

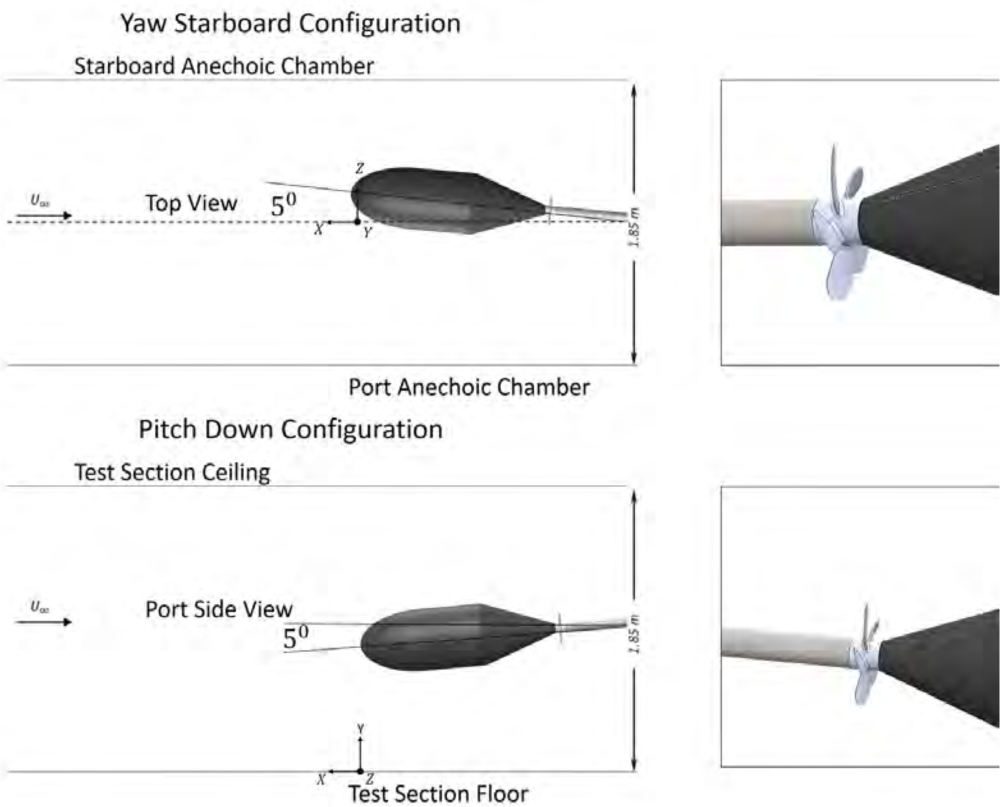

Fig. 1 Schematic of the test section of the Stability Wind Tunnel showing the pitch down and yaw starboard configurations. The top image shows the yaw starboard configuration from a top view and the bottom shows the pitch down configuration as seen from the starboard side wall of the Stability Wind Tunnel.

A test section fixed coordinate system, illustrated in Fig 1, is defined at the mid-span of the test section of the wind tunnel, located on the floor, equidistant from the port and starboard side walls, i.e., at a distance of 0.925 m. The coordinate system is a right-handed Cartesian system, with positive X upstream, Y vertically up, and Z to starboard wall.

B. Body of Revolution (BOR) Model

A thick TBL on the verge of separation is being generated on an aft ramp of a body of revolution as shown in Fig. 2. With a maximum diameter D of 432 mm, the body is made up of three sections: a 2:1 ellipsoidal nose, a 1D long constant diameter section, and 1.17D long 20 degree aft ramp. A 0.81 mm square circumferential trip at the end of the nose (x/D = 0.98) is used to transition the flow. The body of revolution will be inclined at an angle of attack to introduce non-axisymmetric and three-dimensional flow effects.

When installed in the test section the body is supported upstream by 1.6 mm diameter tethers, at the downstream end of the ellipsoidal nose, in a cruciform pattern in the Y-Z plane and supported from downstream with a sting arrangement. A hollow rotating shaft driven downstream by a Kollmorgen AKM54L-ACCNDA00 servomotor through a timing belt is used to drive the propeller. With or without the rotor, body pressure instrumentation cabling is routed from far

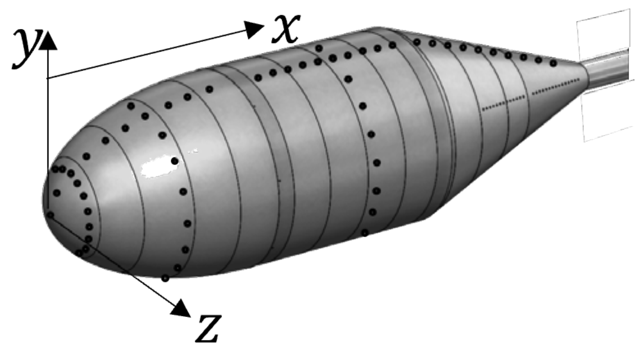

Fig. 2 Schematic of the Body of Revolution (BOR) with it's local coordinates The location of static pressure taps over the BOR surface are shown as black dots.

downstream of the BOR through the shaft so that the rotor inflow is dependent only on the boundary layer generated by the body of revolution and the small wakes generated by the supporting tethers. For details of the drive support and system, see Hickling et. al. [8].

C. BOR Configurations for non-axisymmetric boundary layer development

As the BOR was installed in the test section at $\alpha = 5^o \pm 0.2^o$ angle of attack to generate non-axisymmetric boundary layer over its ramp. This was done using two different configurations: 1) pitch down (5 degree rotation about the Z axis) and 2) yaw starboard (-5 degree rotation about the Y axis). Both configurations are shown in Fig 1.

D. Rotor

The rotor being used in this study is a custom 5-bladed rotor wake adapted to operate at zero thrust at J = 1.44 in the BOR boundary layer when mounted at zero incidence (Fig. 3). The rotor has a diameter of 216 mm (D/2) and a hub diameter of 63.5 mm. The rotor diameter was sized so the blades span is completely immersed in the boundary layer at the end of the BOR (x/D = 3.17). The rotor has no rake but has a 35.5°max sectional skew near the blade tip. At 75 percent of the rotor radius, the blades have a thickness of 6 mm and a chord of 57 mm. The trailing edges of the bladed have 0.188 mm radius to aid in manufacturing.

Fig. 3 CAD of the Zero-Thrust Rotor

E. Coordinate Systems

Acoustic measurements will be presented in terms of the test-section fixed coordinate system of Fig 1. The locations of the rotor disc center and the BOR nose in this system are shown in the Table below.

Configuration	Feature	X [m]	Y [m]	Z [m]
Pitch Down	BOR Nose	0.13	0.69	0.00
	Rotor Disc Center	1.32	0.83	0.00
Yaw Starboard	BOR Nose	0.12	0.89	0.23
	Rotor Disc Center	1.28	0.90	0.10

Table 1 Location of significant physical features of the BOR

PIV results are presented in a body oriented coordinate system. The origin is at the BOR nose (see Fig. 2) with x downstream, y vertically up, and z to port completing a right-handed coordinate system. The xyz and XYZ coordinate system become parallel when the BOR is at 0 °angle of attack. This local coordinate system will be used for each angle of attack in the PIV measurements. The locations of interest are the streamwise oriented xy plane below the body in the pitch down configuration, represented in Fig. 4 by the yellow plane and the rotor inlet profile ($x/D = 3.17$) represented by the dotted line.

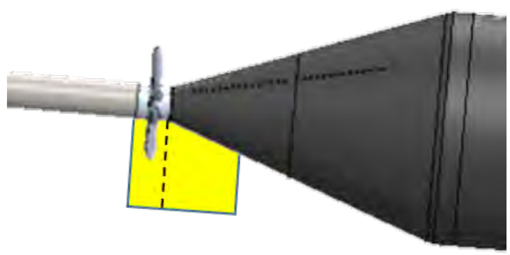

Fig. 4 Streamwise PIV plane showing the location of the velocity field measurement. The measurement region extends from $x/D = 2.9$ to $x/D = 3.3$ in the streamwise direction and down to $y/D = -0.45$

The mean velocity in the x, y, and z directions are defined as U_x, U_y, and U_z respectively and the fluctuating components u_x, u_y and U_z respectively. Given the locally axisymmetric nature of the body of revolution a cylindrical coordinate (r, θ) system is also used where r is measured from the BOR axis and θ is measured from the y axis about the x axis according to the right hand rule.

F. Body Pressure Instrumentation

The body surface pressure is being measured with 85, 0.5 mm diameter pressure taps. A streamwise array of 51 pressure taps measures the streamwise mean surface pressure distribution and two, 16 tap rings on the BOR nose at x/D = 0.5 measure the circumferential uniformity of the mean pressure. The BOR was installed to five degrees angle of attack within ± 0.2°by iteratively adjusting the BOR nose position with the tethers and measuring the resultant mechanical angle of attack using a Digi-Pas DWL-2000 XY digital level. The pressure taps are connected to DTC Initium ESP-32HD acquisition system with a 10" water range and ±0.05 % FS accuracy via Tygon tubes and sampled at 100 Hz. The aerodynamic angle of attack was then confirmed by repeating the iterative process of adjusting the tethers and using the pressure acquisition system to compare the pressure distribution around the circumference of the nose to the Reynolds Averaged Navier Stokes (RANS) calculations performed by Dr Wang's team at the University of Notre Dame.

G. Far-Field Microphone Array

The acoustic field of the rotor is measured with a 251-channel microphone array deployed in the starboard anechoic chamber of the wind tunnel as shown in Fig. 5. This custom-built array employs GRAS type 40PH-S5 ¼" microphones with a dynamic range of 32 to 135 dB(A) and sensitivity of 50 mV/Pa arranged in four interlocking spirals each whose centers are offset in the streamwise direction. In this spiral arrangement, the spacing between microphones is a minimum of 29.8 mm and maximum of 3.82 m.

The plane containing the microphone array sits parallel to the starboard wall of the wind tunnel at a distance of 1.62 m from the mid-span of the test section, i.e., Z = -1.62 m. The coordinates for each of the microphones are show in Fig. 6, with their origin being at the center of the array. All microphones are recorded simultaneously using a custom data acquisition system that allows for external triggering. Data was acquired using all four spirals of the array, however, the results presented in the upcoming sections will refer to the beamforming done using Spiral 2 only (shown as red circles in Fig. 6).

The center of the array (as shown in Fig. 6) is at $X - X_0 = 0.425m$, $Y - Y_0 = 0.866m$, and $Z - Z_0 = 1.616m$ from the origin. All the microphones shown in 6 can be referenced from the origin using this information. Data acquired from the microphones was then used to conduct beamforming. To isolate the turbulence ingestion noise from the unwanted background noise, a smaller integration window was used. An example of the integration windows, focused on the rotor disc for each configuration can be seen in Fig. 7. The contours represent the noise levels at a sample case of 3x BPF during each of those runs.

Fig. 5 AVEC 251-microphone array as seen from behind with a view of the starboard wall of the Stability Wind Tunnel Test Section

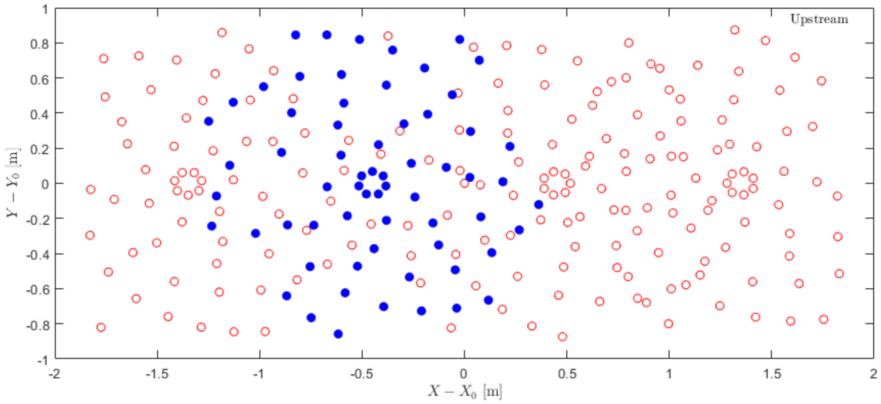

Fig. 6 Relative Far-Field Microphone Array Coordinates from the Array Center. Red circles refer to the location of each microphone within the array. Blue circles indicate the coordinates for microphones in Spiral 2.

H. Particle Image Velocimetry (PIV)

Three-component velocity measurements of the instantaneous inflow to the rotor are being made using the time-resolved, stereo PIV arrangement. In this arrangement, the wind tunnel circuit is seeded with atomized Propylene Glycol with an average particles size of 1 μm and a Photonic Industries DM series laser with a maximum single pulse rate of 25.6 kHz illuminates a y-z plane just ahead of the rotor leading edge plane. Two Phantom v2512 cameras upstream

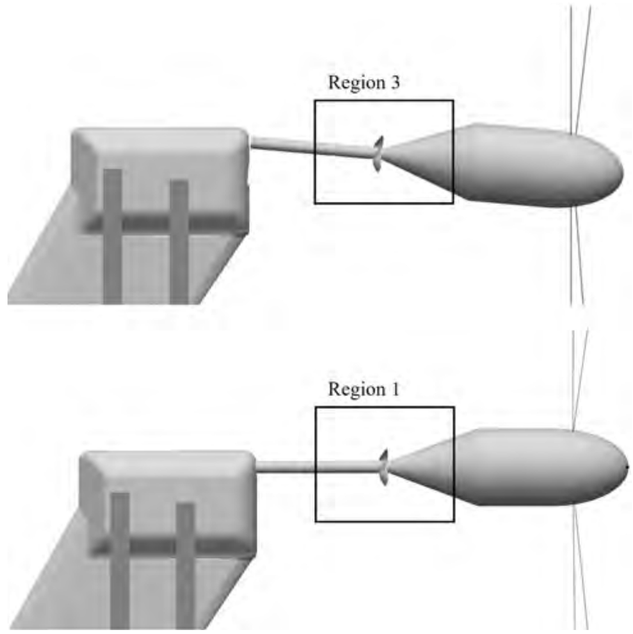

Fig. 7 Size and location of integration window used in beamforming for pitching case (top) and yawing case (bottom).

of the rotor in the test section floor image the laser plane at the bottom of the rotor disc. The cameras and laser are controlled using LaVision Programmable Timing Unit (PTU X) and the data is acquired and processed with DaVis 10.0 software. The PIV, microphone array, unsteady surface pressure, and rotor angular position measurements are synchronized using a trigger signal generated by the PTU.

I. Preliminary RANS Calculations

To aid in the design of the experimental configuration Reynolds Averaged Navier Stokes calculations were computed by Dr Meng Wang's group at the University of Notre Dame for a variety of angles of attack to determine the effects of non-axisymmetry. The results of these calculations informed the chosen 5°angle of attack. The calculations were computed using an ANSYS fluent PISO scheme to second-order accuracy and the turbulence modelled using the $k - \epsilon$ and SST $k - \omega$ models applied after the trip location. The RANS results are used to explain some of the PIV flow field findings.

The turbulent kinetic energy ($TKE = \sqrt{\overline{u_x^2} + \overline{u_y^2} + \overline{u_z^2}}$) at the rotor plane as a function of y and z are plotted in Fig. 8. The measured PIV plane relative to the RANS results is shown by the orange line.

IV. Results and Discussion

Most measurements were conducted at a Reynolds number based on body diameter $Re_D = 600,000$, corresponding to a free stream velocity between 20 and 23.5 m/s depending on flow temperature. For the analysis conducted in this

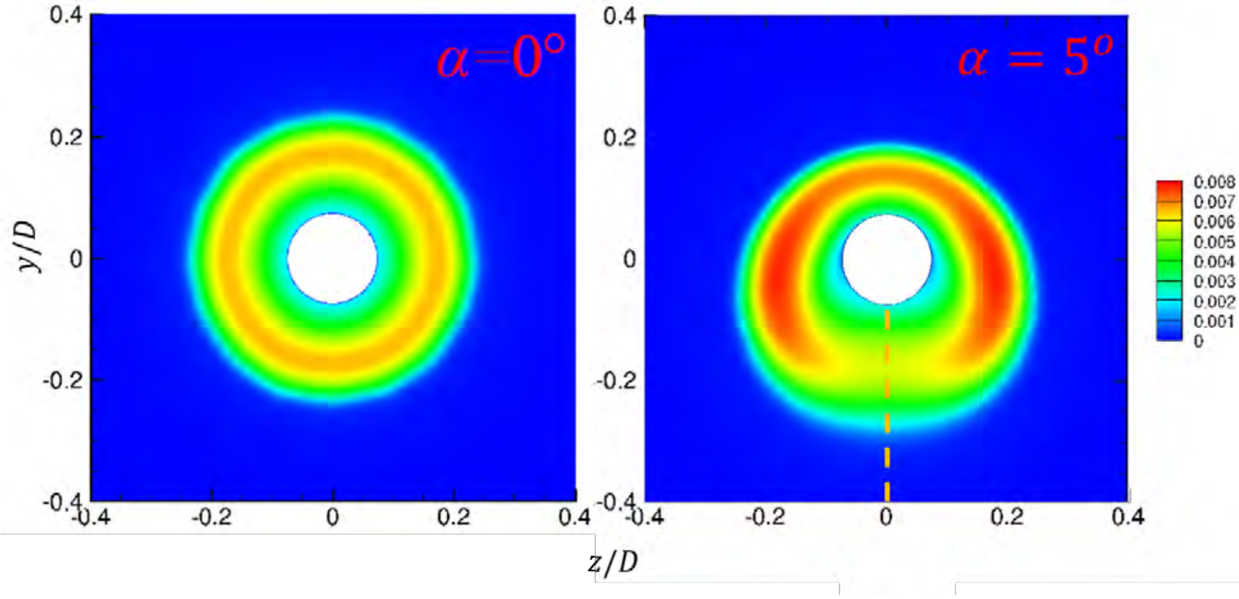

Fig. 8 RANS calculations for the turbulent kinetic energy in the radial plane courtesy of Dr Meng Wang of UND

paper, this Reynolds number will be considered as the standard case. The rotor was designed to operate at a maximum of 5000 RPM, which limited the advance ratio offered by the rotor for the given Reynolds number. Therefore, the cases of low advance ratios, which would have required the rotor to turn at a rate higher than 5000 RPM were instead conducted at a lower freestream Reynolds number, i.e. Re_D = 500,000. Table 2 shows the details for the cases where PIV measurements were conducted.

Table 2 Advance ratios and Reynolds numbers for PIV measurements

Advance Ratio, J	Re_D
1.10	500,000
1.27	600,000
1.34	600,000
1.44	600,000
2.64	600,000

Several additional advance ratios spread between 0.86 (highly thrusting) to 2.64 (highly braking) were also studied using acoustic measurements, however only a select range of advance ratios will be discussed in the analysis presented in the coming sections. These advance ratios were achieved in two different ways:

1- By adjusting the rotor speed, while keeping the freestream velocity (Reynolds number) constant.

2- By adjusting the freestream velocity (Reynolds number) of the flow, while keeping the rotor speed constant.

The data for both these methods of advance ratio adjustments is analyzed and presented in Section IV.D.

A. Mean flow at the Lee-side Rotor Inlet for J=1.44

The data presented show significant three dimensional and non-axisymmetric effects resulting from boundary layer roll up on the leeward side of the body. There have been several studies documenting the formation of a pair of counter rotating vortices induced by inclining a body of revolution at an angle of attack as discussed in the Introduction ([10], [11], and [12]). These vortices have significant effects on the mean flow and turbulence within the measured PIV plane.

The contours shown in Fig.9 and Fig. 10a reveal the mean flow at the zero thrust condition for the non-axisymmetric condition and compare it to the axisymmetric case investigated by Balantrapu [9]. Examining the velocity profiles in Fig.10b at $x/D = 3.17$ we see some significant differences in the U_x and U_y (streamwise and spanwise) components. There is little change to the U_z component due to the flow field being mostly symmetric about the measured plane. There is evidence of the boundary layer thickening in how much further up the profile the U_x component reaches the edge velocity when compared to the axisymmetric case. The gradient of the U_x component $\frac{\partial U_x}{\partial y}$ is decreased for the non-axisymmetric case. There are significant increases in the U_y component closer to the wall for the non-axisymmetric case.

The boundary layer thickness was determined to be where the turbulence intensity ($I_{uu} = \sqrt{\overline{u^2}/U_\infty^2}$) fell below 1.5%. Examining the boundary layer (shown by the dark black line) we see significant thickening for the non-axisymmetric flow case ($\delta = 109mm$ compared to $\delta = 75mm$). This finding is consistent with the RANS results which qualitatively show an increase in the thickness of the boundary layer on the leeward side of the body and a decrease in thickness on the windward side.

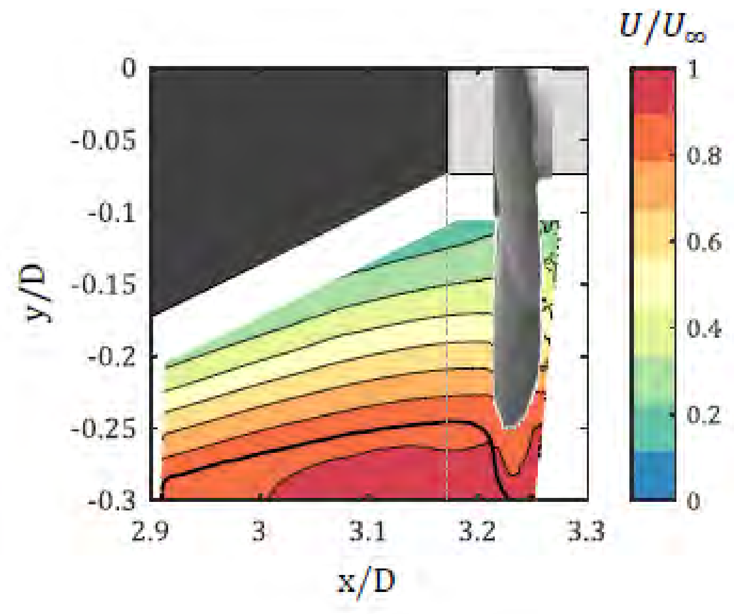

Fig. 9 Axisymmetric mean flow with boundary layer thickness shown by a solid dark line. Data obtained from [9].

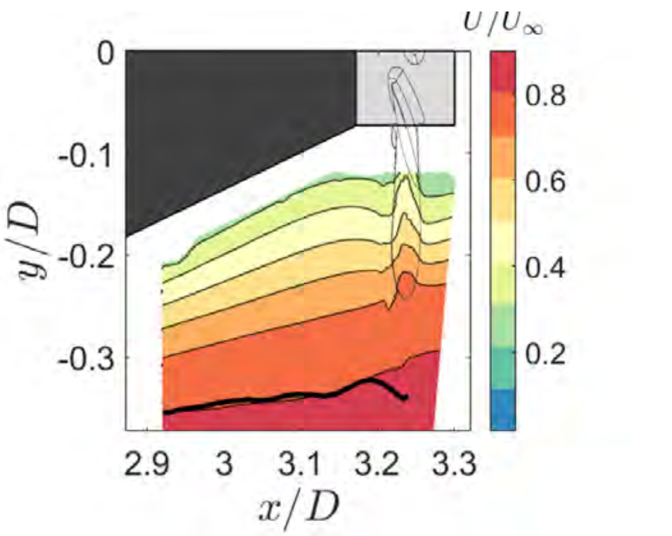

(a) Non-axisymmetric mean flow with boundary layer thickness shown by a solid dark line

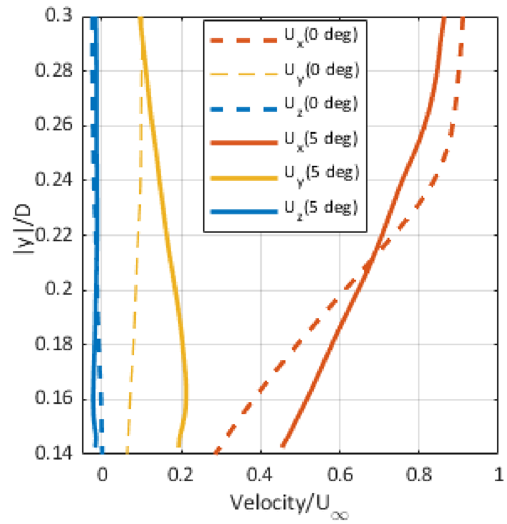

(b) Mean velocity profiles at $x/D = 3.17$ where the dotted lines are the axisymmetric results from [9] and the solid lines are data obtained from the pitch down configuration test

Fig. 10 Boundary Layer Thickness, Mean Flow, and Boundary Layer Profiles

B. Turbulence in a Non-Axisymmetric Boundary Layer

The expectation from the RANS results seen in Fig. 8 was that the turbulence in the measured plane would be reduced by the vortex roll up. We see turbulence in the measured plane shows significant departure from the axisymmetric case. Fig. 11 shows a comparison of the $\overline{u_x^2}$, $\overline{u_y^2}$, and $\overline{u_z^2}$ profiles as a function of distance from the BOR surface at the rotor inlet plane for a zero thrust advance ratio. In general the turbulence levels are approximately half the turbulence levels in the axisymmetric case. It can be seen that the axisymmetric case shows significant turbulence peaks at $|y|/D = 0.18$. However these peaks are not evident in the non-axisymmetric case. There is, however, a distinct three peak behaviour being exhibited in the $\overline{u_x^2}$ (or streamwise) component of the Reynolds Stress. This is evident in both Fig. 11 and 12a. The overall turbulence levels are also significantly reduced in this plane. This can likely be attributed to the non-axisymmetric effects of a pair of counter-rotating streamwise vortices. These form due to boundary layer rollup on the leeward side of a body of revolution when inclined at a significant angle of attack. The turbulence levels are reduced due to lower turbulence freestream being brought into the leeward side as visible in the RANS results in Fig. 8.

Fig. 12a and 12b show contours of the premultiplied spectra for the non-axisymmetric case and the axisymmetric case investigated in [9]. These represent the contribution of each frequency to the turbulent energy within the flow normalized on the edge velocity, freestream and body diameter. The frequency normalized on the body diameter and edge velocity is shown logarithmically on the horizontal axis and the distance from the rotor hub normalized on the boundary layer thickness δ is shown on the vertical axis. The axisymmetric flow case in Fig. 12b has a clearly defined peak occurring at approximately 0.5δ that can also be seen in the turbulence profiles in Fig. 11. In comparison

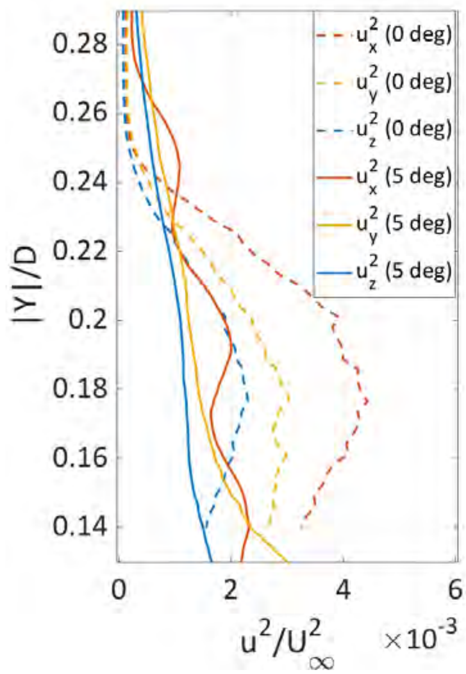

Fig. 11 Comparison of Reynolds Stress Profiles for Axisymmetric and Non-Axisymmetric BOR at the Rotor Inlet for J=1.44

the non-axisymmetric flow case shows spectral peaks at various locations in the boundary layer. The peaks occur at $0.25\delta, 0.5\delta$, and 0.7δ at two frequencies, $2U_e/D$ and $5.5U_e/D$. This multi-peak behaviour of the turbulence is repeated in Fig. 11 and further explored in the next section.

C. Effects of Thrust on the Velocity Field

Examining the effects of varying the thrust gives insight into the three peak turbulence stress shape. Fig. 13a shows the contours of the ratio between the normalized mean flow at two thrust conditions; zero thrust (J=1.44) and high thrust (J=1.10). The rotor effects can clearly be seen just upstream of the rotor with an increase in the mean contours and a distortion of the upstream isolines. There are streaks of high relative velocity shown in Fig. 13a that stretch upstream of the rotor that correspond to the points in the Reynolds stress profiles where the difference in the stress intensity is highest. This is evidence that the multi-peak turbulence stress shape is a rotor effect. This is further corroborated by inspection of the turbulence profile (Fig. 13b) and the location of the rotor; the rotor tip extends to $|y|/D = 0.25$ and the streamwise turbulence $\overline{u_x^2}/U_\infty^2$ rapidly decreases to 0 at this location.

It is posited that the angle of the flow relative to the rotor inflow plane is the main driver of the turbulence profile structure. As mentioned in Section III.D the rotor is wake adapted to the axisymmetric configuration where the zero thrust condition occurs at J=1.44. By changing the angle of the BOR with respect to the freestream the rotor is no longer operating in an axisymmetric wake. As the rotor thrust increases, the velocity at the inlet plane increases and the

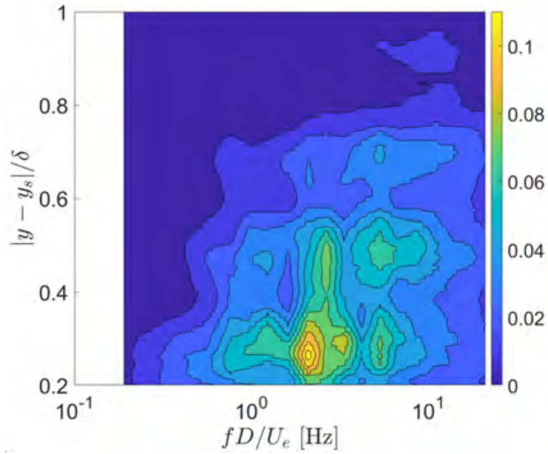

(a) Pre-multiplied spectra for the non-axisymmetric case using phase mean subtraction to remove the effect of the rotor

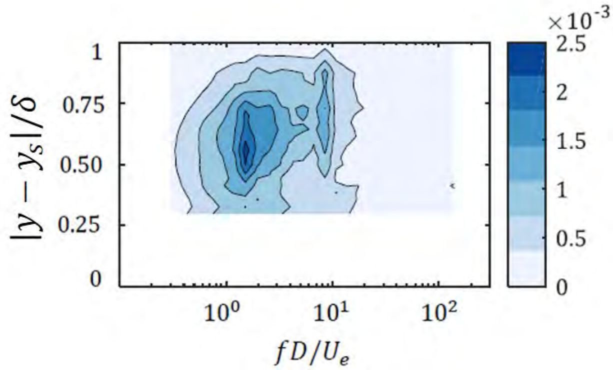

(b) Pre-multiplied spectra for the axisymmetric case using time mean subtraction

Fig. 12 Pre-multiplied spectra contours where the horizontal axis is frequency normalized on the edge velocity and body diameter, the vertical axis is distance from the rotor hub normalized on the boundary layer thickness and the contours of $fG_{u_x u_s}$ are normalized on the freestream velocity, edge velocity and body diameter, $\frac{f\,G_{u_x u_x}}{U_\infty^2}(\frac{U_e}{D})$.

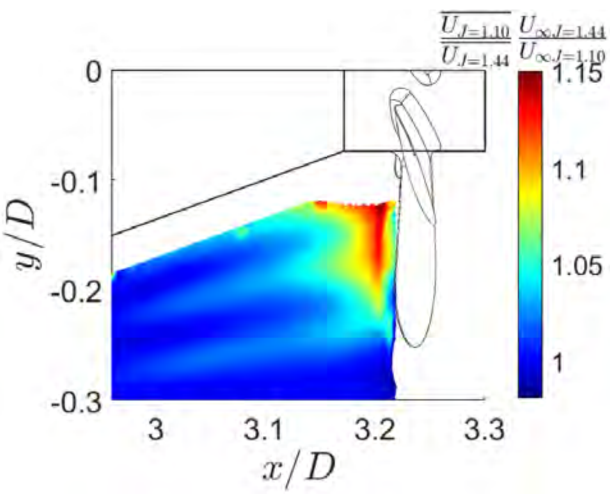

(a) The ratio of the mean velocity field at J=1.10 to J=1.44

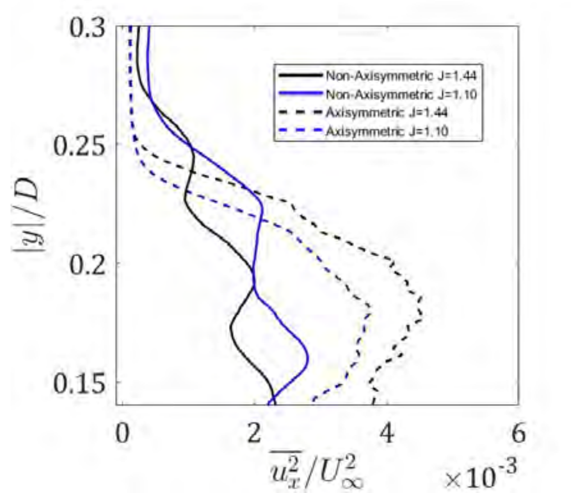

(b) Mean Velocity Profiles at $x/D = 3.17$. Solid lines are the non-axisymmetric case, dotted lines are the axisymmetric case.

Fig. 13 Thrust comparisons for J=1.44 and J=1.10

pressure gradient becomes more favourable. This naturally acts to reduce the turbulence within the flow. If the thrust along the radius of the rotor blade varies significantly (and indeed it does as shown by Fig. 13a) then the turbulence will also vary along that profile, with peaks and troughs at the low and high thrust locations respectively. This result combined with the multi-peak behaviour of the turbulence stress in Fig. 11 suggests that J=1.44 is no longer the zero thrust condition.

The autospectrum for the streamwise velocity normalized on the freestream velocity was computed for several locations ($|y|/D = 0.225$, $|y|/D = 0.188$, and $|y|/D = 0.125$) within the rotor inlet plane and plotted for frequencies from 10 Hz to 7 kHz in Fig. 14. Comparing Fig. 14a to Fig. 14b we see a spectral tone at the blade passage frequency

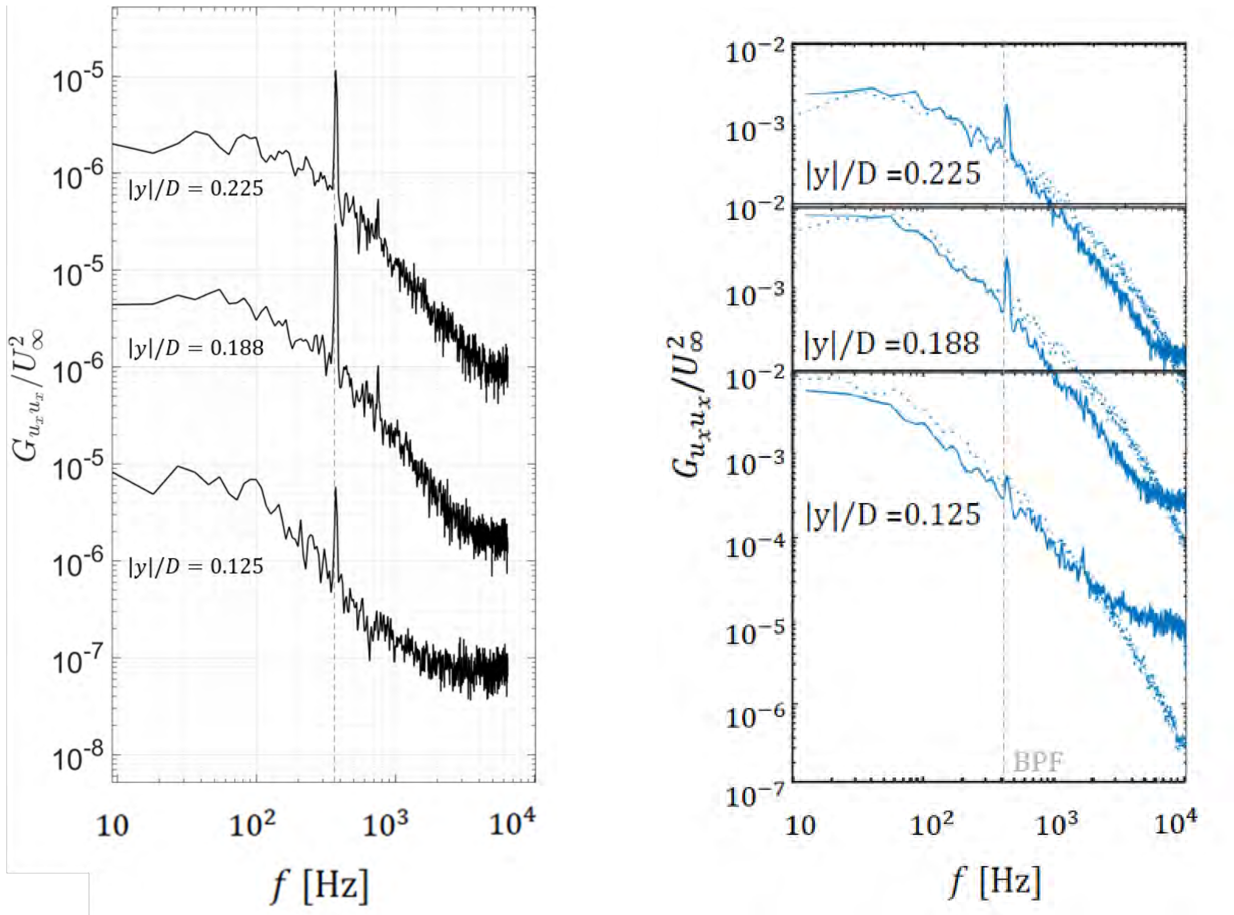

(a) Non-axisymmetric auto-spectrum

(b) Axisymmetric auto-spectrum

Fig. 14 A comparison of the streamwise velocity auto-spectrum taken at three locations in the rotor plane $|y|/D = 0.225$**,** $|y|/D = 0.188$**, and** $|y|/D = 0.125$

clearly indicating the streamwise velocity is significantly affected by the rotor passage. The blade passage frequency peaks for the axisymmetric auto-spectrum contribute a lower spectral energy to the overall spectral energy than the non-axisymmetric rotor passage peaks. It is evident that moving towards the surface of the BOR in the axisymmetric case the turbulence begins to overwhelm the effect of the rotor and the BPF peak appears depressed. The same trend is seen in the non-axisymmetric case except the rotor's contribution to the overall spectral energy is significantly higher relative to the turbulence contribution. This can be explained by realizing that, as discussed in the previous paragraph, this is no longer a zero thrust condition so the rotor is actively altering the flow structure. Furthermore the turbulence at this plane is significantly lower than for the axisymmetric case as seen in Fig. 11. These both contribute to the more dominant BPF frequency.

D. Angle of Attack effects on Rotor Noise

The absence of axisymmetry in the development of the turbulent boundary layer over the ramp of the BOR results in uneven ingestion of turbulence into the rotor, i.e. the boundary layer thickness was not the same around the circumference of the BOR exit, see Fig 8. For the standard freestream condition at $Re_D = 600,000$, the variation in the advance ratio from $J = 1.1$ (Thrusting) to $J = 1.44$ (Zero-Thrust) can be seen in Fig 15. Fig 15a shows the results for zero thrust (J = 1.44). Here the x-axis shows frequency normalized on the Blade Passage Frequency (BPF) for this case. The y-axis shows the spectral noise levels that have been normalized on the product of the square of the mean freestream and the cube of the blade relative velocity, and then experssed in terms of SPL. The red curve represents the data from the zero-pitch and zero-yaw case as shown by Hickling et. al. [8]. The blue curve shows the far-field sound spectrum for the pitch down case. Sound levels are within a dB of those measured with the BOR at zero angle of attack at most frequencies. This is obtained by integrating the beamform maps over the integration windows shown as Region 3 in Fig 7. All beamform maps were examined before integration to verify that the rotor was the dominant source of sound. The view of the rotor in this position is shown on the diagram inset in the bottom right of Fig 1. Here, the rotor blades are roughly perpendicular to the observer direction as they pass through the lee-side of the BOR through the region where the boundary layer is thicker but less turbulent than at zero angle of attack, or elsewhere in the rotor disk, as revealed in Figures 8 and 11. The green curve shows the same results for the yawed configuration, where the BOR is turned towards the array. Sound levels seen from this angle are elevated by 1 to 5dB above those seen at zero angle of attack. For this condition, the rotor blades are roughly perpendicular to the observer as they pass through the thickest part of the boundary layer as revealed in the RANS results presented in Fig 8. The perspective of the rotor blades, as seen from the center of the Spiral 2 array (Fig 6) is shown inset top right of Fig 1.

All the three curves described in the previous paragraph show a decreasing trend with frequency, with significant rounded peaks at the multiples of the Blade Passage Frequencies (BPFs). These accumulation of high noise levels, slightly right-shifted from their respective multiples of the BPFs are the haystacks, as pointed out by Hickling et. al. [8]. As the rotor thrust is increased and the advance ratio reduces (Fig 15(b), (c) and (d)), both the directivity effects and the haystacks observed at J=1.44 become more prominent. The haystacks result from the multiple cutting of elongated turbulence structures by successive rotor blades and, at higher thrust, the turbulence is likely to be stretched as it is drawn into the rotor accentuating this effect. We expect that further analysis of the PIV results will explicitly reveal this effect.

Another feature of the spectra that is not visible in Fig 15 are the tonal peaks that occurred at the shaft harmonics and their multiples, generated by parasitic noise from the rotor drive system. These peaks were removed by linearly averaging the noise levels corresponding to two frequency bands below and above the shaft harmonic frequency. Another feature detected through the far-field acoustic measurements is the singing nature of the tethers used to support the suspended

BOR in the test section. These tethers were mounted at a normalized streamwise distance x/D ≈ 1 and then routed to two separate locations each at the floor and the ceiling, as shown in Fig 1. The 1.6mm -diameter tethers mounted in tension acted as vortex-shedding cylinders with a specific shedding frequency for each run. The expected shedding frequency was determined by approximating the Strouhal number as 0.2 and finding the frequency corresponding to the freestream velocity experienced by the tethers for each run of the experiment. This feature is not visible in Fig 15, however it manifests itself in the contours shown in Fig 16 and 17.

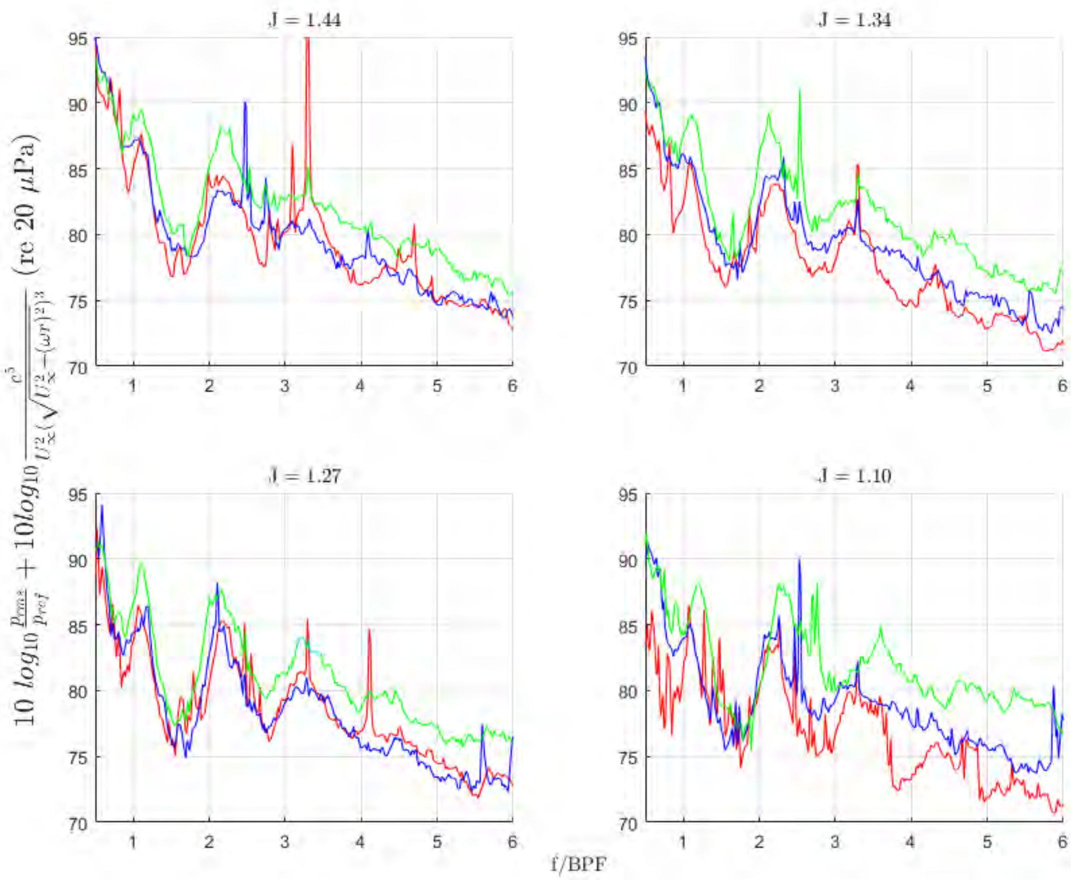

Fig. 15 Effects of advance ratio variation on rotor noise with BOR at various configurations. α = 0^o **(red),** α = 5^o **Pitch (blue),** α = 5^o **Yaw (green)**

As discussed earlier, the rotor advance ratio was controlled in two different ways: 1) by adjusting the rotor speed, keeping the freestream velocity constant, and 2) by adjusting the freestream and keeping the rotor speed constant. Since the noise levels were scaled on both these characteristics, (i.e., the freestream and the blade relative velociy), their individual effects were normalized for comparisons. Fig. 16 shows the comparison between the pitch (left) and the yaw (right) configuration for the case when the advance ratio was adjusted by controlling the freestream velocity. For both these experiments, the Reynolds number based on the BOR diamater (Re_D) was chosen to be 600,000 similar to Hickling, et. al. [8]. For the pitching case, the mean freestream velocity was kept at 23.77 m/s while for the yaw case this was kept at 23.75 m/s. The variation in the freestream velocity occured due to the change in the ambient temperature and pressure, since the tests were conducted on separate days. Once again, the noise levels are scaled with the blade relative velocity and the freestream turbulence.

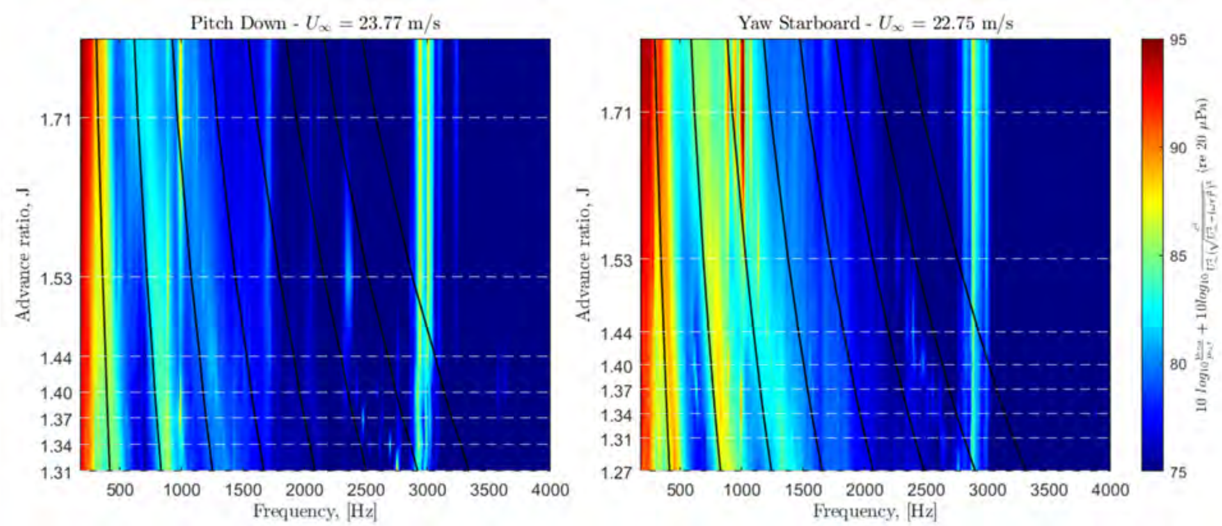

Fig. 16 Contours of the Normalized Noise Level Spectra with variation in advance ratio at Constant Freestream. The solid black lines represent multiples of the Blade Passage Frequencies (BPF) at each advance ratio. The dashed white lines represent the advance ratios at which data was taken during the experiment

Fig 16 shows the contours of the noise levels for advance ratios ranging from 1.31 (thrusting) to 1.71 (braking). The frequency is shown on the x-axis while the y-axis shows the advance ratios. The advance ratios used in this experiment are labelled with their corresponding values and are shown as white-dashed lines running horizontally through the plot. The levels of the contours show the SPL, i.e. noise levels normalized on the product of their respective freestream velocity and the blade relative velocity, as described in the earlier section for Fig 15. The freestream velocity corresponding to the standard case, i.e. $Re_D = 600,000$ is shown on top of each plot in Fig 16. At lower frequencies, the ambient noise from the surroundings of the facility dominate the entire test section as is shown in the contours as a sharp red vertical strip. A sudden jump in the noise levels is observed at broadband frequencies just above the Blade Passage Frequencies (BPF), shown as solid black lines in Fig 16 corresponding to each advance ratio. This evidently displays the presence of broadband haystacks as a result of the rotor cutting through the coherent structures within the boundary layers multiple times, as shown by Hickling, et. al. [8]. The slope of the black lines is a result of the variation of the rotor speed to adjust the advance ratio, while keeping the freestream constant. Another feature observed in the contour show presence of tonal noise at around 3 kHz. This feature does not follow the slope created by the BPF line, and results due to the singing nature of the support tethers (1.6 mm in diameter) present in the test section for the stabilizity and support of the BOR. Since this closely agrees with the expected value of the shedding frequency for the corresponding freestream of 23.8 m/s and a Strouhal number of 0.2, it can be confirmed that this is indeed tether noise. This is also seen in the contours for the yawed case.

Once again, due to the directivity of the Turbulence Ingestion Noise, the contours for the yaw case (right) are more prominent and occur at higher levels as compared to the pitch case (left). The presence of the haystacks at the third and even fourth multiple of the BPF is also much more significant for the yaw case. This further supports the strong directionality of the noise, since for the yaw case, the far-field microphone array is in the direction of the rotor where it receives sound from where the blades are cutting the most turbulent portions of the flow.

A similar observation can be made for the case when the advance ratio was controlled by adjusting the freestream velocity, keeping the rotor speed at a constant. Fig. 17 shows the comparison between the pitch (left) and yaw (right) case. Similar to Fig. 16, the presence of haystacks are observed blue-shifted from the multiples of the Blade Passage

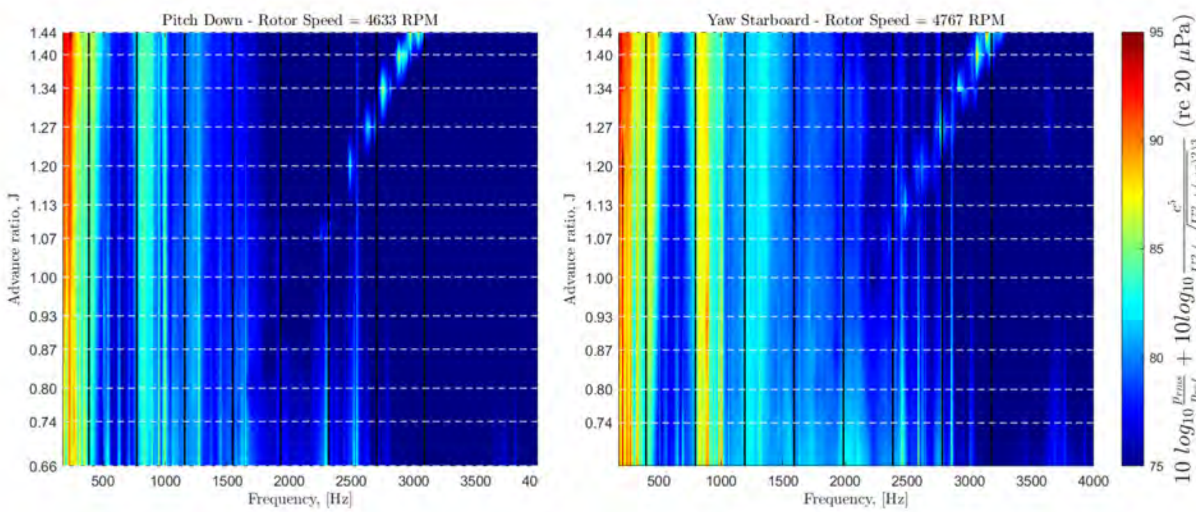

Fig. 17 Contours of the Normalized Noise Level Spectra with variation in advance ratio at Constant Rotor Speed. The solid black lines represent multiples of the Blade Passage Frequencies (BPF) at each advance ratio. The dashed white lines represent the advance ratios at which data was taken during the experiment

Frequency. For the pitching case, the rotor was set to rotate at 4633 rotations per minute (BPF = 386 Hz). The constant BPF for all the advance ratio resulted in a purely vertical solid black line in 17. Similarly, for the yaw case, the rotor was kept at 4767 RPM (BPF = 397 Hz). Contrary to Fig. 16, we can see a higher resolution of advance ratio due to the fact that higher values of advance ratio could be achieved by decreasing the freestream for this test. The similar levels of high thrust (low-advance ratio) were not possible by continuously increasing the rotor speed because of the limitations of the rotor to spin at a maximum design speed of 5000 RPM. Once again, the effects of the directivity are clearly evident as the presence of haystacks in the yaw case (right) are significant and clearly visible for as much as the sixth multiple of the Blade Passage Frequency. The fingerprints of the tether noise are also visible in the contours, however, they are visible only at higher advance ratios (high freestream velocities) and gradually disappear as the freestream velocity drops. The presence of the tether noise at a slope in both contours of Fig. 17 also indicate the variation in the shedding frequency of the circular cross-section tethers.

Both Fig. 16 and 17 show a spike in the noise levels at extremely low frequencies. The presence of high levels of noise at those frequencies are a result of background ambient noise from the various electrical components present around the test section. The blue shift from the multiples of the Blade Passage Frequencies in both figures is about 7 to 12%.

V. Conclusion

Measurements of a turbulent boundary layer ingested into a rotor at the aft of a body of revolution inclined at angle of attack were taken. Velocity fields and acoustic measurements were taken and the results compared to previous axisymmetric flow studies. For the plane measured by the PIV in the pitch down configuration there were significant three dimensional effects. These acted to increase the boundary layer thickness and significantly dampen the turbulence levels when compared to the axisymmetric case. For the non-axisymmetric case the turbulence profiles take on a three peak structure. This is likely due to the thrust variation along the rotor span as the effect was noted to increase with advance ratio. Confirmation of the three turbulence peaks was shown in the premultiplied auto-spectrum plots, these peaks were shown at $0.25\delta, 0.5\delta$, and 0.7δ in the rotor plane. The streamwise autospectrum showed that the spectral energy at the blade passage frequency was more dominant over the turbulence when compared to the axisymmetric case. The acoustic analysis showed an increase in the sound power levels with advance ratio as well a consistent 5 dB increase for the non-axisymmetric yaw case. This was attributed to the rotor directivity; the sound experienced by the observer will be dominated by the turbulent structures being cut by the rotor blade facing the microphone array. This occurred when the rotor blade was below the BOR. For the pitch down case the plane underneath the BOR was the least turbulent, therefore the sound was reduced. For the yaw starboard case the plane underneath the BOR was significantly more turbulent than both the axisymmetric case and the pitch down case, resulting in higher SPL. For all cases (axisymmetric, pitch, and yaw) haystacking was seen with the peaks blue shifted 7-11%.

Acknowledgments

The authors would like to thank the Office of Naval Research for sponsoring this work under grants N00014-17-1-2698 and N00014-17-1-2682, specifically Drs. Ki-Han Kim and John Muench. Authors are particularly grateful to Dr Meng Wang and his team at UND for the RANS CFD results that provided context to these data. Further acknowledgements go to Vidya Vishwanathan, Shishir Damani, Rachel Andrews, Aayush Salot, and Shivam Khullar amongst others for their assistance during the wind tunnel experiments. The authors would also like to thank Mr. Michael Marcolini for his ever present advice.

References

[1] Sevik, M., "Sound Radiation from a Subsonic Rotor Subjected to Turbulence," *NASA-SP-304*, 1974, pp. 493–512.

[2] Blake, W., *Mechanics of Flow Induced Sound and Vibration*, Academic Press, Orlando, FL, 1986.

[3] Hanson, D., "Spectrum of Rotor Noise Caused by Atmospheric Turbulence," *Journal of the Acoustical Society of America*, Vol. 56, No. 1, 1974, pp. 110–136.

[4] Majumdar, S., and Peake, N., "Noise Generation by the Interaction between Ingested Turbulence and a Rotating Fan," *Journal of Fluid Mechanics*, Vol. 359, 1998, pp. 181–216.

[5] Atassi, H. M., and Logue, M., "Fan Broadband Noise in Anisotropic Turbulence," , 2009. https://doi.org/10.2514/6.2009-3148.

[6] Anderson, J. M., Catlett, M. R., and Stewart, D. O., "Modeling Rotor Unsteady Forces and Sound Due to Ingestion of Spatially Inhomogeneous Turbulence," , May 30 to June 1 2016. https://doi.org/10.2514/6.2016-2735.

[7] Anderson, J. M., Catlett, M. R., and Stewart, D. O., "Modeling Rotor Unsteady Forces and Sound Due to Homogeneous Turbulence Ingestion," *AIAA Journal*, Vol. 53, No. 1, 2015, pp. 81–92. https://doi.org/10.2514/1.j052874.

[8] Hickling, C., Balantrapu, N. A., Alexander, W. N., Millican, A. J., Lowe, K. T., Devenport, W. J., and L., G. S. A., "Turbulence Ingestion into a Rotor at the Rear of an Axisymmetric Body," , May 20-23 2019.

[9] Balantrapu, A. N., "The Space-time Structure of an Axisymmetric Turbulent Boundary Layer Ingested by a Rotor," 2021.

[10] Kumar, P., and Prasad, J. K., "Side force over slender body with rings at different location at subsonic speed," *Proceedings of the Institution of Mechanical Engineers, Part G: Journal of Aerospace Engineering*, Vol. 231, No. 8, 2016, pp. 1478–1491. https://doi.org/10.1177/0954410016654180.

[11] E., T. B., and A., C. Q., "An Investigation of the Normal-Force and Vortex-Wake Characteristics of an Ogive-Cylinder Body at Subsonic Speeds," *NASA Technical Note D-1297*, 1962.

[12] J., R. E., "Real Flow Over a Body of Revolution at Angle of Attack," 1953.

[13] Devenport, W. J., Burdisso, R. A., Borgoltz, A., Ravetta, P. A., Barone, M. F., Brown, K. A., and Morton, M. A., "The Kevlar-walled anechoic wind tunnel," *Journal of Sound and Vibration*, Vol. 332, No. 17, 2013, pp. 3971–3991. https://doi.org/10.1016/j.jsv.2013.02.043.